PAPER • **OPEN ACCESS**

Investigating the impact of intermediate-mode perturbations on diagnosing plasma conditions in DT cryogenic implosions via synthetic x-ray Thomson scattering

To cite this article: H Poole *et al* 2025 *Plasma Phys. Control. Fusion* **67** 015034

OPEN ACCESS
IOP Publishing
Plasma Physics and Controlled Fusion
Plasma Phys. Control. Fusion **67** (2025) 015034 (10pp)
https://doi.org/10.1088/1361-6587/ad9e74

Investigating the impact of intermediate-mode perturbations on diagnosing plasma conditions in DT cryogenic implosions via synthetic x-ray Thomson scattering

H Poole[1,2,*], D Cao[3], R Epstein[3], I Golovkin[4], V N Goncharov[3,5], S X Hu[3], M Kasim[6], S M Vinko[1], T Walton[4], S P Regan[3] and G Gregori[1]

[1] Department of Physics, University of Oxford, Oxford OX1 3PU, United Kingdom
[2] Department of Physics and Astronomy, University of Rochester, Rochester, NY 14627, United States of America
[3] Laboratory for Laser Energetics, University of Rochester, Rochester, NY 14623, United States of America
[4] Prism Computational Sciences, Madison, WI 53711, United States of America
[5] Department of Mechanical Engineering, University of Rochester, Rochester, NY 14611, United States of America
[6] Machine Discovery, Oxford OX4 4GP, United Kingdom

E-mail: hannah.poole@rochester.edu

Received 30 July 2024, revised 19 November 2024
Accepted for publication 12 December 2024
Published 30 December 2024

Abstract

The pursuit of inertial confinement fusion ignition target designs requires precise experimental validation of the conditions within imploding capsules, in particular the density and temperature of the compressed shell. Previous work has identified x-ray Thomson scattering (XRTS) as a viable diagnostic tool for inferring the in-flight compressed deuterium-tritium shell conditions during capsule implosions (Poole *et al* 2022 *Phys. Plasmas* **29** 072703). However, this study focused on one-dimensional simulations, which do not account for the growth of hydrodynamic instabilities. In this work, two-dimensional DRACO simulations incorporating intermediate-mode perturbations up to Legendre mode $\ell = 50$ were used to generate synthetic XRTS spectra with the SPECT3D code. The analysis employed Markov-Chain Monte Carlo techniques to infer plasma conditions from these spectra. The results demonstrate that the XRTS diagnostic platform can effectively discern the in-flight compressed shell conditions for

* Author to whom any correspondence should be addressed.

targets with varying adiabats, even in the presence of intermediate-mode perturbations. This work underscores the potential of XRTS for realistic inertial confinement fusion experiments, providing a robust method for probing the complex dynamics of fusion implosions.

Keywords: x-ray Thomson scattering, Inertial confinement fusion, DT cryogenic implosions, Bayesian analysis

1. Introduction

The experimental demonstration of target gain in inertial confinement fusion (ICF) implosions at the National Ignition Facility (NIF) has been realised in recent years [1, 2]. While direct-drive ICF approaches have yet to demonstrate target gain, recent work has reported hydro-equivalent burning plasmas on OMEGA at the Laboratory for Laser Energetics [3]. This accomplishment is the result of a series of mitigation strategies, complemented by diagnostic techniques, including neutron [4–6] and x-ray imaging [7, 8], as well as advancements in target development [9, 10]. The design of ICF targets is heavily aided by radiation-hydrodynamic simulations capable of modelling the multiphysics involved in capsule implosions [11–13] and statistical mapping methods [14, 15].

The ignition of the deuterium–tritium (DT) fuel requires achieving sufficient temperatures and areal densities to create self-heating by alpha particles. For an ICF capsule to ignite, the areal density, ρR, of the hot spot formed at stagnation must satisfy the condition [16, 17],

$$\rho R \times T_i \gtrsim 0.3\,g\,\mathrm{cm}^{-2} \times 5\,\mathrm{keV}. \tag{1}$$

The areal density of the hot spot is controlled by varying the entropy of the fuel, which is determined by the shell adiabat, defined as the ratio of the shell pressure, P_{Shell}, to the Fermi-degenerate pressure [18]. For DT fuel, the shell adiabat is given by [19],

$$\alpha_{\mathrm{fuel}} \simeq \frac{P_{\mathrm{Shell}}\,[\mathrm{Mbar}]}{2.2\,(\rho\,[\mathrm{g\ cm}^{-3}])^{5/3}}\,. \tag{2}$$

A lower adiabat value (and thus a larger hot spot areal density) reduces the minimum laser energy required to achieve ignition. However, targets imploded on a low adiabat are more susceptible to instability growth [20]. Therefore, optimising the target adiabat is a crucial aspect of ICF research [21, 22], with recent OMEGA capsules focusing on moderate adiabat ($\alpha_{\mathrm{fuel}} \sim 5$) designs [3, 23].

On many ICF implosions conducted at both the NIF and OMEGA, asymmetries in the capsule convergence have been observed to severely affect overall target performance [24, 25]. These asymmetries can result from imperfections in the laser drive and target and are characterised by their Legendre mode number $l = 2\pi R/\lambda_p$, where the perturbation wavelength λ_p is measured relative to the initial target radius R. Low mode perturbations are associated with large-scale features compared to R, such as misaligned drive beams. These perturbations can be amplified by the growth of hydrodynamic instabilities, degrading the performance of the ICF implosion [26].

Validating hydrodynamic simulations for direct-drive ignition target designs requires experimental platforms capable of effectively probing and characterising the density and temperature conditions of the high-energy-density implosions. One promising technique for achieving this is spectrally-resolved x-ray Thomson scattering (XRTS) [27, 28]. While XRTS has demonstrated success on probing CH capsule implosions [29, 30] and liquid deuterium [31, 32], it has not yet been fielded on a layered, cryogenic DT ICF implosion. Previous work demonstrated XRTS as a viable diagnostic tool for diagnosing the compressed deuterium-tritium shell conditions in direct-drive ICF implosions [35]. Utilising one-dimensional (1-D) LILAC simulations, the temperature and density conditions of two extreme target adiabats were resolved. However, 1-D simulations cannot capture the hydrodynamic instabilities, such as the Rayleigh-Taylor instability, that arise during realistic ICF capsule implosions. Consequently, the conditions in these implosions can differ significantly from those predicted by 1-D simulations, potentially impacting the analysis of collected XRTS data. Therefore, it is essential to assess how these hydrodynamic instabilities might influence the plasma conditions inferred through the XRTS technique before conducting such experiments. Such a study can provide confidence in the application of this diagnostic technique to realistic capsule implosions.

In this work, the effects of intermediate-mode perturbations on inferring the in-flight compressed shell conditions using synthetic XRTS are investigated. The analysis is conducted by constructing synthetic, spatially integrated spectra using the collision-radiative code SPECT3D [33], which serves as a post-processor for the two-dimensional (2D) radiation hydrodynamic code DRACO [13]. Reverse Monte Carlo techniques are employed to determine the compressed shell conditions from the resultant spectra.

2. Proposed experimental setup

The experimental platform investigated in this work, as illustrated in figure 1, utilises the setup as proposed in [35]. The probing x-rays are produced assuming a 1 kJ laser with a 10 ps pulse length incident on a backlighter foil placed 0.5 cm away from the imploding target. Assuming an x-ray conversion efficiency of $\eta_x = 0.01\%$ and a spectral bandwidth of $\Delta E_{\mathrm{ph}}/E_{\mathrm{ph}} = 5 \times 10^{-3}$, this backlighter setup generates $\approx 3 \times 10^{14}$ photons

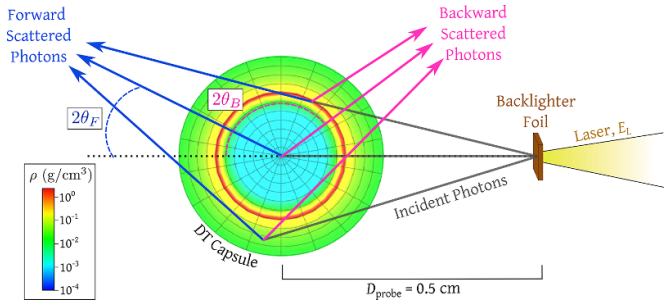

Figure 1. Schematic of the experimental setup based on the configuration proposed in [35]. The density profile of the DT capsule is shown at the in-flight conditions investigated. The forward and backward spectrometers are situated at $2\theta_F = 40^\circ$ and $2\theta_B = 120^\circ$, respectively. Reproduced from [35]. CC BY 4.0.

at $E_{\text{ph}} = 2$ keV. Such a backlighter energy could be generated using a silicon He-α, or aluminium K-α transitions.

To characterise the inelastic scattering features observed on a spectrally-resolved x-ray scattering power spectrum, it is beneficial to compare the scale length interrogated by the incident x-ray photons to the characteristic scale length for correlations between electrons. This comparison is defined as the scattering parameter [34],

$$\alpha = \frac{1}{k\lambda_s}, \tag{3}$$

where the scattering vector for a probe of wavelength $\lambda_i = hc/E_{\text{ph}} \approx 0.6$ nm collected at a scattering angle of 2θ is,

$$k = \frac{4\pi \sin\theta}{\lambda_i}. \tag{4}$$

The electron screening length, λ_s, is determined as,

$$\lambda_s = \sqrt{\frac{k_B T_e \epsilon_0}{n_e e^2} \frac{\mathcal{F}_{1/2}(\eta_e)}{\mathcal{F}_{-1/2}(\eta_e)}}, \tag{5}$$

where $\mathcal{F}_j(\eta_e)$ is the normalised jth order Fermi–Dirac integral [36] of the dimensionless chemical potential, $\eta_e = \mu_e/k_B T_e$.

Whilst the screening length can be determined analytically via equation (5), for conditions such as those found in warm dense matter plasmas an effective temperature, T_{eff}, which interpolates between the classical and degenerate regimes is often employed [37]. The scattering parameter can therefore be determined as,

$$\alpha = \frac{\lambda_i}{4\pi \sin\theta} \sqrt{\frac{e^2 n_e}{\epsilon_0 k_B T_{\text{eff}}}}, \tag{6}$$

$$T_{\text{eff}} = \sqrt{T_e^2 + \left(\frac{T_F}{1.3251 - 0.1779\sqrt{r_s}}\right)^2}, \tag{7}$$

where $T_F = \hbar^2 \left(3\pi^2 n_e\right)^{2/3}/2m_e k_B$ is the Fermi temperature and $r_s = (3/4\pi n_e)^{1/3}/a_B$ is the ratio of average inter-particle spacing to the Bohr radius, a_B.

When the scattering parameter $\alpha > 1$, the power spectrum reflects the coherent scattering from the plasma, arising from the collective motion of the electrons. The scattering spectrum therefore exhibits resonances at the characteristic frequency of the wave-like fluctuations in the electron density, commonly referred to as electron plasma waves. The position of this resonance is governed by the plasmon dispersion relation. In the regime of weak degeneracy, where the plasma degeneracy is defined as the ratio of the electron's thermal to Fermi energy, E_F,

$$\Theta = \frac{k_B T_e}{E_F} = k_B T_e \left[\frac{2m_e}{\hbar^2 \left(3\pi^2 n_e\right)^{2/3}}\right], \tag{8}$$

the plasmon dispersion relation is given by [38],

$$\omega^2 = \omega_{\text{pe}}^2 + 3k^2 v_{\text{th}}^2 \left(1 + 0.088 n_e \Lambda_e^3\right) + \left(\frac{\hbar k^2}{2m_e}\right)^2. \tag{9}$$

Here, $\omega_{\text{pe}}^2 = e^2 n_e/\epsilon_0 m_e$ is the plasma frequency, $v_{\text{th}}^2 = k_B T_e/m_e$ is the mean electron thermal speed and Λ_e is the thermal de Broglie wavelength.

The non-collective scattering regime is characterised by $\alpha \ll 1$. In this regime, the incident probe undergoes scattering due to the motions of individual particles, as the length scale probed is smaller than the characteristic screening length. The free-free scattering features therefore reflects the shape of the momentum distribution. Consequently, the frequency shift of a scattered photon by a free electron is given by,

$$\omega = -\frac{\hbar k^2}{2m_e} \pm \mathbf{k} \cdot \mathbf{v}. \tag{10}$$

In weakly degenerate systems, the width of the Compton scattering spectrum can provide a measure of the electron temperature.

To minimise the uncertainty on the inferred conditions, it is beneficial to design an experimental platform that accesses both x-ray scattering regimes. As illustrated in figure 1, this is achieved using a single x-ray probe in conjunction with two detectors: one positioned in the forward scattering regime, at $2\theta_F = 40^\circ$, and the other in the backward scattering regime, at $2\theta_B = 120^\circ$. The selection of the incident wavelength is crucial, as the scattering parameter's dependency on this wavelength necessitates the use of a relatively low x-ray photon energy to access the collective scattering regime. However, too low an x-ray energy will prevent the scattering being observed above the target self-emission and additionally restrict the backward scattering detector's access to the non-collective regime.

In previous work utilising 1-D simulations, x-ray probes with photon energies of $E_{\text{ph}} = 2$ keV and $E_{\text{ph}} = 3.5$ keV were investigated. However, the introduction of hydrodynamic instabilities in the current study necessitates a focus on the lower energy probe. At relatively constant electron temperatures, the significant presence of lower-density plasma can lead to non-collective features observed in the forward detector.

Selecting the lower energy probe therefore reduces the contamination in the forward detector from non-collective scattering features.

3. Generating synthetic scattering

The cryogenic DT simulations were calculated using the 2D radiation-hydrodynamics code DRACO [13, 39]. DRACO is an arbitrary Lagrangian–Eulerian code operating in cylindrical coordinates with axial symmetry, and employs a 3D ray-trace model for the laser drive (deposition is azimuthally averaged) that also accounts for cross-beam energy transfer [40]. Similar to LILAC [41], it also uses the first-principles equation of state [42] tables and first-principles opacity tables [43] for material models, while using the implicit Schurtz-Nicolai-Busquet for nonlocal electron heat-transport model [44].

In this investigation, the 2D simulations incorporated multi-modal perturbations from OMEGA's beam-port geometry (laser illumination $\sigma_{\rm rms} \approx 0.2\%$), beam-power imbalance (beam energy $\sigma_{\rm rms} \approx 3.3\%$), ice surface roughness ($\sigma_{\rm rms} \approx 0.9\ \mu$m), and laser-imprint up to Legendre mode $\ell = 50$. While laser-imprint smoothing by spectral dispersion (SSD) [45] was also included, the implosion was made more perturbed by reducing the SSD bandwidth to only 10% of what OMEGA actually delivered, effectively increasing the simulated laser-imprint amplitude by almost 2x over nominally expected levels.

The targets modelled in these simulations were selected to replicate the in-flight adiabat conditions studied in [35], with an additional target featuring an in-flight adiabat of 5.4 to serve as a benchmark for distinguishing between closer adiabats. The target designs, detailed in table 1, comprised a CD ablator encasing a DT ice layer and the DT fuel. The investigated in-flight stage of the capsule implosion is defined as the point of two-thirds convergence, where the outer surface of the ablated DT shell has been compressed to two-thirds of the initial radius of the DT gas, $R_{\rm Ablation\,surface}/R_{\rm Vapour,\,initial} = 2/3$.

The impact of including intermediate-mode instabilities on the density of the in-flight compressed shell is illustrated in figure 2. These 2D instabilities reduce the uniformity of the compressed shell, effectively dispersing the DT mass over a broader distribution. Such a deviation from the ideal, comparatively homogeneous 1-D scenario can ultimately affect convergence around representative conditions, as a wider range of plasma conditions influences the observed scattering spectra. This is because the number of detected photons in the free-free x-ray scattering feature depends on the electron density [28, 46],

$$N_{\rm d} = \left(\frac{E_L}{h\nu}\eta_x\right)\left(\frac{\Omega_{\rm plasma}}{4\pi}\eta_{\rm att}\right)\left[\frac{n_e\sigma_{\rm Th}l}{(1+\alpha)^2}\right]\Gamma_{\rm det}\,. \tag{11}$$

Here, E_L is the energy of the laser incident on the foil backlighter, $\Omega_{\rm plasma}$ is the solid angle of the plasma as seen by the backlighter, $\eta_{\rm att}$ is the attenuation of the probe x-rays through the dense plasma, l is the path length of the photons through the plasma and $\Gamma_{\rm det}$ gives the fraction of scattered photons detected. The $\Gamma_{\rm det}$ accounts for the solid angle of the detector, the reflectivity of the Bragg crystal and the detector quantum efficiency. For this work, as in [35], a $\Gamma_{\rm det} \sim 10^{-5}$ is assumed.

Table 1. Radial thicknesses for each component of the simulated target designs.

Adiabat	CD ablator (μm)	DT ice (μm)	DT gas (μm)
2.7	8	50	376
5.4	8	41	431
8.8	8	39	430

The mass-averaged properties from the 2D simulations are determined by,

$$\langle F\rangle = \frac{\sum F_i\,\rho_i\,2\pi\,r_i A_i}{\sum \rho_i\,2\pi\,r_i A_i}\,, \tag{12}$$

where F is the desired plasma property and A_i is the area of cell i. The mass-averaged electron densities in the compressed shell region for each target are compared to the corresponding probability distribution functions at the investigated in-flight stage in figure 3(a). The contribution of each zone from the simulation to the electron density probability distribution is weighted by its mass (i.e. $\rho_i 2\pi\,r_i A_i$). To identify the contributing scattering regimes in the forward detector, a similar weighting procedure is performed to determine the probability distribution of the scattering parameter in the compressed shell, as shown in figure 3(b). This analysis indicates that, despite the increased density distributions, the forward detector is dominated by collective scattering observations throughout the compressed shell. However, the lowest adiabat target, with the densest shell, exhibits the largest mean scattering parameter, while the highest adiabat shows a tail of contributions from regions where $\alpha \sim 1$.

The synthetic scattering spectra were generated by post-processing the 2D DRACO simulations with SPECT3D [33, 35]. SPECT3D is a spectroscopy code that computes radiative transfer equations along a series of line-of-sight to each detector through the plasma grid. At each plasma volume along a line-of-sight, it determines the observed scattered power spectrum using an x-ray scattering simulator [47, 48], given an input x-ray source. This allows SPECT3D to predict the fully spatially integrated spectra while accounting for plasma opacity, geometric effects and target self-emission.

At present, SPECT3D does not incorporate any detector considerations into the modelled x-ray scattering signal. Careful consideration must therefore be given to model the expected spectral resolution and number of photons in the free-free scattering feature. Utilising equation (11) and taking a representative density of $n_e \approx 5\times10^{23}$ cm^{-3} and path length of $l \approx 50\,\mu$m, gives $N_{\rm d} \sim 500$. Assuming a spectral resolution of 3 eV bin^{-1} the scattering intensities as shown in figure 4 are produced. Over the 10 ps pulse of the x-ray backlighter, as observed in figure 4(a), the expected inelastic scattering to background self-emission signal ratio is ≈ 1.5.

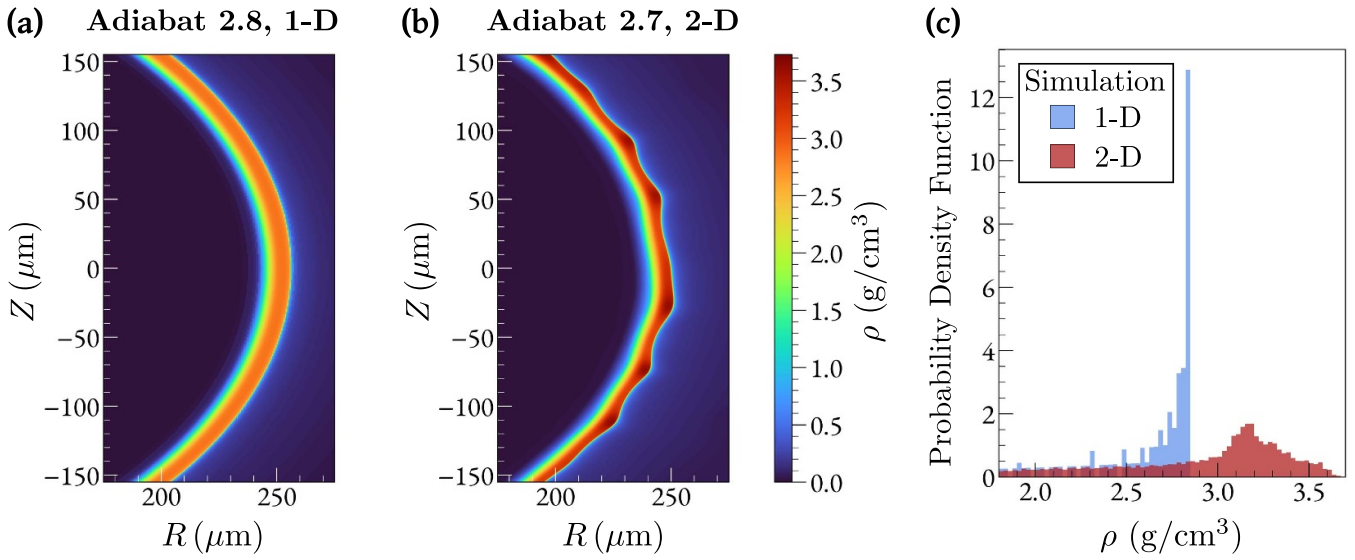

Figure 2. Mass density profiles of the compressed DT shells at two-thirds convergence for similar adiabat cases using 1-D, (a), and 2D, (b), models. The 1-D adiabat, as investigated in [35], consists of a 8 μ m thick polystyrene ablator surrounding a 57 μm thick DT ice layer and 368 μm of DT gas. The 2D target details are provided in table 1. (c) The probability density function of the mass density within the compressed DT shell for both the 1-D (blue) and 2D (red) cases.

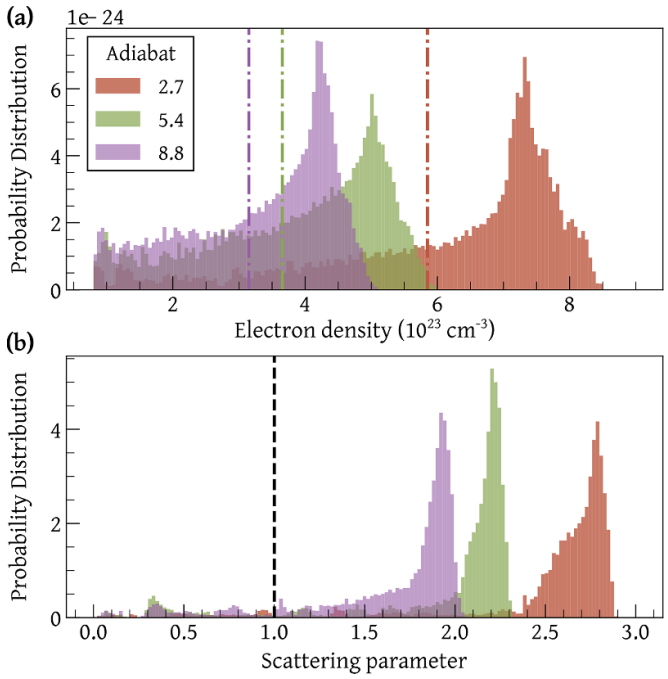

Figure 3. Probability distribution functions of the electron density, (a), and scattering parameter α, (b), in the compressed shell region for each adiabat target investigated with each zone's contribution weighted by its mass ($\rho_i 2\pi\, r_i A_i$). The scattering parameter was determined assuming an x-ray probe of 2 keV and scattering angle of 40°. The dash-dotted vertical lines in (a) indicate the mass-averaged electron density in the compressed shell region for each target. The black dashed vertical line in (b) indicates the transition point between the collective ($\alpha > 1$) and non-collective ($\alpha \ll 1$) scattering regimes.

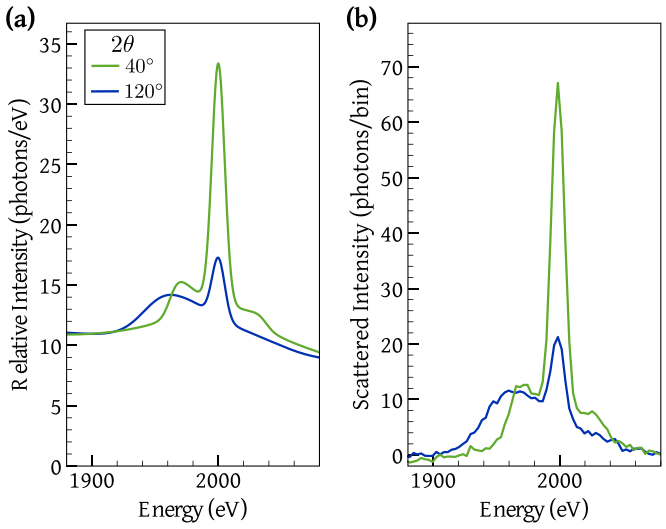

Figure 4. (a) Total relative detected signal produced by SPECT3D for the target with an in-flight adiabat of 5.4. The signal is integrated over the time of the x-ray pulse, $\Delta t = 10$ ps. (b) Synthetic experimental x-ray scattering data, where the background self-emission has been removed. These are produced assuming a spectral resolution of 3 eV bin^{-1} and Poisson noise.

Furthermore, synthetic experimental noise was incorporated into each spectrum. This involved applying Poisson statistics, which estimates the noise as $\sim 1/\sqrt{N_t}$, where N_t is the total number of photons per spectral resolution element, including self-emission.

One method to evaluate the impact of intermediate-mode perturbations on the scattering spectra is to isolate contributions from each plasma region in the comparable 1-D and 2D simulations shown in figure 2. The plasma regions, as illustrated in figure 5(a), are defined as the unshocked DT gas, compressed DT shell, coronal DT plasma and ablator plasma. The boundary between the DT shell and the hot DT plasma is defined at the density threshold of $\rho_{\max}/e$. In both the forward

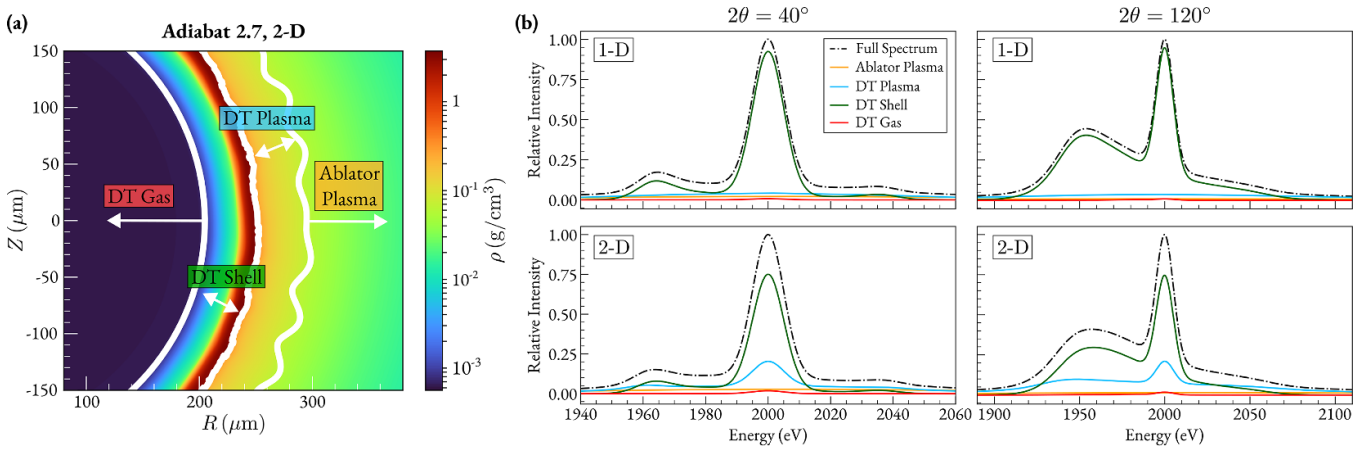

Figure 5. (a) 2D mass density profile, as illustrated in figure 2(b), with distinct plasma regions highlighted by white interface borders. (b) Comparison of simulated scattering contributions from each plasma region for both forward and backward detectors, using the 1-D and 2D models of the capsule implosion as depicted in figure 2.

and backward scattering features presented in figure 5(b), a notable contribution from the DT plasma region is evident in the 2D case. This arises from the increased density in the DT plasma due to hydrodynamic perturbations. It is therefore crucial to assess whether this feature results in inferred plasma conditions that are no longer representative of the DT compressed shell.

4. In-flight Conditions

Inferring the conditions from the synthetic experimental signal requires a forward fitting model capable of exploring the large parameter space, $\Psi(n_e, T_e, Z)$, whilst addressing the inverse problem instability. The inverse problem instability implies that a measured spectrum can be fitted equally well by a range of different conditions [49], which is particularly challenging when modelling such an inhomogeneous environment. A Markov-Chain Monte Carlo (MCMC) procedure has been shown to be a robust approach for exploring complex multi-parameter simulations [35, 49, 50]. This method uses Bayesian inference to determine the likelihood of a set of parameters producing the observed spectrum, $I_{\text{exp}}(\omega)$, based on an acceptance probability $P[I_{\text{exp}}(\omega)|\Psi] = \text{e}^{-\beta_{\text{cost}}}$. A standard cost function, β_{cost}, used to assess the appropriateness of each fit determines the maximum error between the forward-fitted spectrum, $I_{\text{fit}}(\omega)$, and the synthetic experimental spectrum [49],

$$\beta_{\text{cost}} = \max\left[\frac{I_{\text{fit}}(\omega) - I_{\text{exp}}(\omega)}{\sqrt{2}\sigma}\right]^2. \tag{13}$$

Here, σ is the standard deviation representative of the noise of the synthetic scattering spectrum.

Utilising a cost function, as outlined in equation (13), to achieve optimal fits to data necessitates experimental signals that exhibit relatively uniform intensities across the frequency space of interest. This approach is particularly suitable for the scattering signals observed in the backward non-collective scattering regime, where the elastic and inelastic scattering signals typically remain within a factor of two of each other, as illustrated in figure 4. However, for certain spectra, such as those observed by the forward scattering detector, where the elastic scattering signal exceeds the inelastic signal by a factor of five, the cost function in equation (13) can preferentially fit the more intense elastic scattering signal. This presents a problem, as crucial information about the plasma conditions is derived from the inelastic scattering signal.

To address this issue, a 'percentage' cost function is utilised instead,

$$\beta_{\text{cost}} = \max\left[\frac{I_{\text{fit}}(\omega) - I_{\text{exp}}(\omega)}{I_{\text{exp}}(\omega)}\frac{1}{\sqrt{2}\sigma}\right]^2. \tag{14}$$

This form of the cost function provides a more balanced assessment of the fit to both the elastic and inelastic peaks, resulting in fits that better represent the data and, consequently, the plasma conditions.

Accurately modelling the inhomogeneous plasma poses a challenge. As illustrated in figure 5(b), multiple distinct regions within the capsule implosion contribute to the overall scattering signal, with a broad range of plasma conditions contributing to the observed spectrum within each region. This observation suggests that an optimal fit to the scattering spectrum could, in theory, be achieved by fitting multiple distinct plasma conditions. However, this approach introduces several complications.

Firstly, it is not feasible to spectrally isolate the contributions from the distinct plasma regions, meaning an experimentally produced scattering signal will have to be analysed as a whole. Secondly, while it is possible to fit two or more sets of conditions to the entire spectrum, this approach would require restrictive constraints on the parameter ranges explored by the MCMC analysis—such as limiting on set of conditions to a specific temperature range. Allowing the multiple conditions to explore overlapping parameter spaces will lead to poor MCMC convergence, as each condition set will attempt to fit both high- and low- temperature conditions.

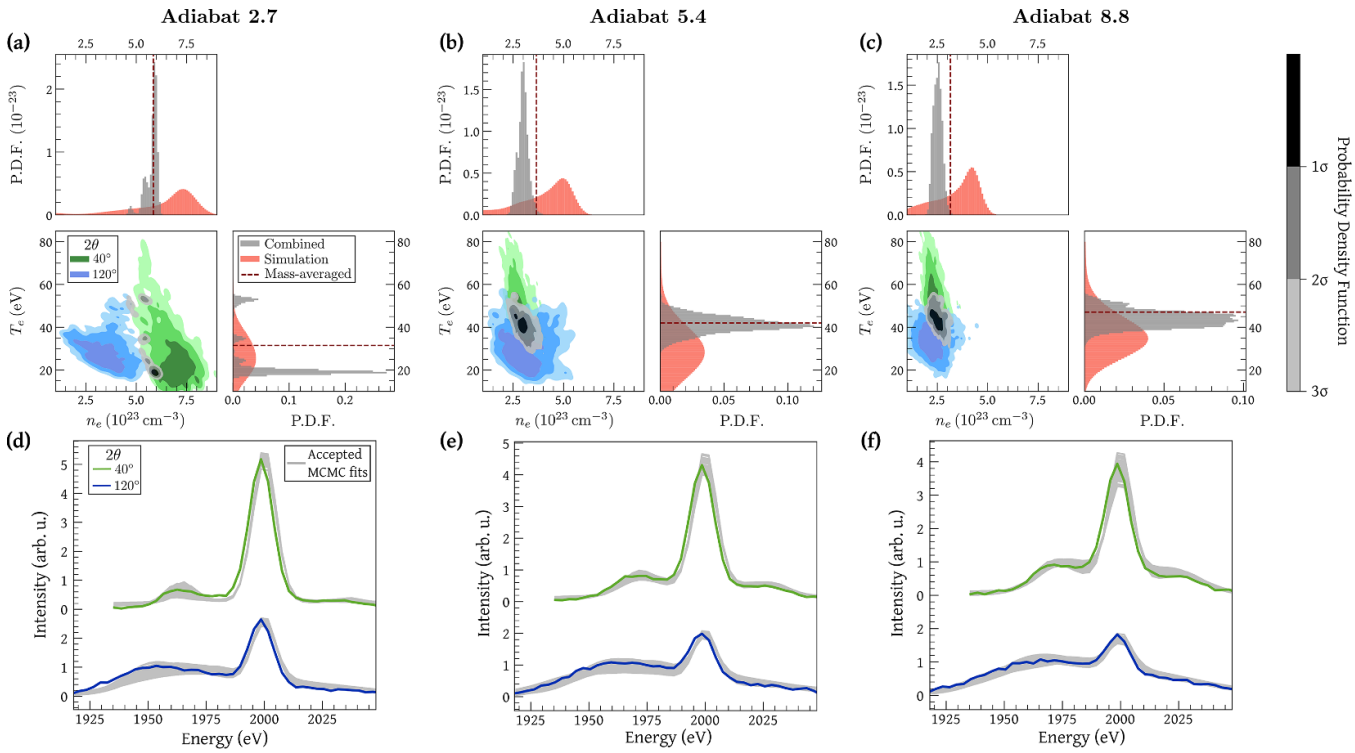

Figure 6. MCMC convergence of electron density and temperature for 2D simulations using a 2 keV probe. The variation in DT plasma parameters are shown for; (a) 2.7 adiabat, (b) 5.4 adiabat, and (c) 8.8 adiabat target designs. The lower quadrant plots compare the 1, 2, and 3σ parameter correlations for the MCMC converged forward (green) and backward (blue) detector scattering analysis. Utilising equation (15), the corresponding combined distributions are superimposed as grey heat maps. The diagonal histograms compare the combined probability densities for each parameter (in grey) to the compressed shell simulation distributions (in red). The mass-averaged parameter values from the 2D simulations are highlighted as a red dashed lines. Below each matrix the corresponding accepted MCMC fits for the forward and backward scattering are shown compared to the corresponding synthetic simulated spectrum.

Imposing restrictions on parameter exploration to prevent this overlap would introduce implicit biases, as these restrictions would need to be informed by simulations due to the lack of detailed experimental data on conditions across different implosion regions. As this diagnostic technique aims to enable independent benchmarking of simulations rather than a reliance on them, the most objective approach is to analyse the spectra assuming a single set of average conditions. This simplification allows for an assessment of whether this approach can still yield valuable insights into the compressed shell conditions, despite spectral contributions from other plasma regions.

The MCMC analysis explored the ionisation, temperature and density space for the forward and backward scattering spectra individually. For the DT region, the parameter space assumed a uniform distribution with linear sampling for the electron temperature, $1 \leqslant T_e(\mathrm{eV}) \leqslant 10^3$ and ionisation, $0 \leqslant \bar{Z} \leqslant 1$ (where $\bar{Z} = (Z_D + Z_T)/2$). Logarithmic sampling was used for the electron density, $10^{20} \leqslant n_e(\mathrm{cm}^{-3}) \leqslant 5 \times 10^{24}$. This extensive parameter space was chosen to minimise bias in the converged conditions.

For any cost function, β_{cost}, the value of σ is typically not known *a priori*. It is chosen for each MCMC exploration such that the synthetic scattering signal falls comfortably within the spread of the accepted fits. For the forward scattering analysis, the cost function utilised a σ of 6×10^{-2} with equation (14), while a σ of 5×10^{-4} was chosen for the backward scattering analysis utilising equation (13). Examples of the range of accepted MCMC fits are shown in the lower grid of figure 6. While each synthetic scattering spectrum may not precisely align with the range of MCMC fits, this discrepancy is an inherent outcome of modelling an inhomogeneous scattering event using a single uniform plasma region.

The converged probability density functions, $\mathrm{Pr}(n_e, T_e)$, are illustrated for each target in the upper grid of figure 6 and listed in table 2. While the ionisation state was explored, each MCMC analysis converged around $\bar{Z} > 0.9$, and the ionisation probability distribution functions are omitted for simplicity. Given the 2D density and temperature probability density functions for the forward and backward scattering spectra, shown in green and blue in figure 6, respectively, a combined probability can determined as [50],

$$\mathrm{Pr}_j(n_e, T_e) = \frac{\mathrm{Pr}_f(n_e, T_e) \times \mathrm{Pr}_b(n_e, T_e)}{\sum_{n_e, T_e} \left[\mathrm{Pr}_f(n_e, T_e) \times \mathrm{Pr}_b(n_e, T_e)\right]}, \qquad (15)$$

where the subscripts f and b denote the forward and backward scattering fits, respectively. These combined probability density functions are superimposed in figure 6 as grey heat maps.

Table 2. The converged MCMC fitting parameters, as illustrated in figure 6, are compared with the mass-weighted compressed shell parameters obtained from the 2D simulations. The results are presented for both the forward and backward detector analyses, as well as their combined distributions.

	$\mathbf{n_e}$ (cm^{-3})	$\mathbf{T_e}$ (eV)
	Adiabat 2.7	
Simulation	5.9×10^{23}	32
40°	$(6.9 \pm 0.6) \times 10^{23}$	24 ± 9
120°	$(3.4 \pm 0.7) \times 10^{23}$	28 ± 6
Combined	$(5.8 \pm 0.3) \times 10^{23}$	25 ± 12
	Adiabat 5.4	
Simulation	3.7×10^{23}	42
40°	$(2.8 \pm 0.3) \times 10^{23}$	47 ± 7
120°	$(3.0 \pm 0.7) \times 10^{23}$	29 ± 7
Combined	$(3.0 \pm 0.3) \times 10^{23}$	41 ± 4
	Adiabat 8.8	
Simulation	3.2×10^{23}	47
40°	$(2.3 \pm 0.2) \times 10^{23}$	54 ± 7
120°	$(2.2 \pm 0.4) \times 10^{23}$	34 ± 6
Combined	$(2.5 \pm 0.2) \times 10^{23}$	44 ± 4

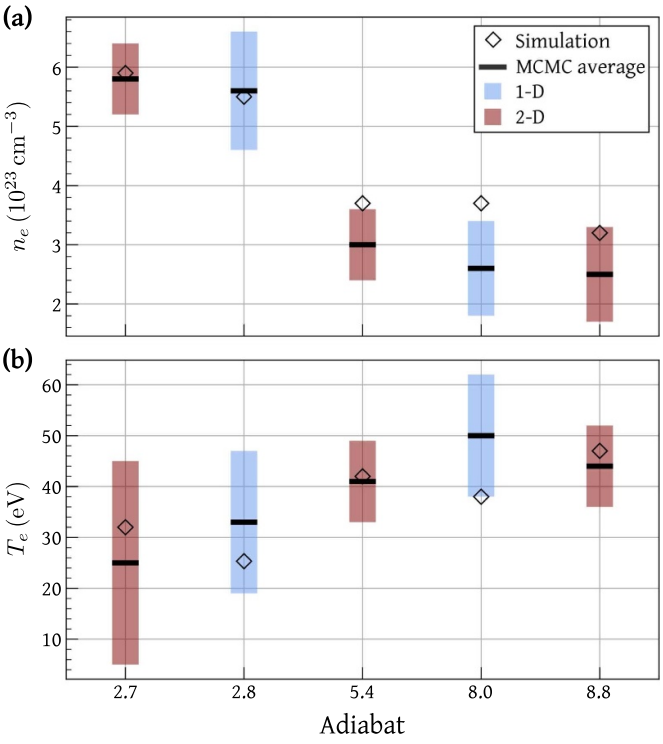

Figure 7. Comparison of combined MCMC parameter convergence for electron density, (a), and electron temperature, (b) using 1-D ([35]), in blue, and 2D, in red, simulations with a 2 keV x-ray probe. The error bars shown are the 2σ errors from the combined MCMC probability distribution functions. The mass-averaged compressed shell values determined from each simulation are indicated as black diamonds.

5. Discussion

Overall, there is good agreement between the combined probability distribution functions and the mass-averaged simulation conditions of the compressed shell. To evaluate the effectiveness of the XRTS technique developed both in this work and in [35] for discerning plasma conditions within the in-flight compressed shell, the range of converged MCMC parameters across the investigated adiabats is presented in figure 7. As the adiabat serves as a practical measure of the shell's plasma conditions (as defined in equation (2)), selecting targets that cover the broad range of adiabats used in direct-drive ICF implosions enables an investigation into whether this technique can reliably resolve temperature and density information about the compressed shell across the various implosion conditions observed in DT cryogenic implosions. For both the 1-D and 2D simulations, a noticeable disparity emerges in the inferred electron density between low- and high-adiabat targets. Although the shift in electron temperature across the adiabat range is not as pronounced, this technique adeptly captures the trend of resolving higher temperatures for higher adiabats.

The expected variation in shell conditions within a specific adiabat are much smaller than the overall density and temperature range illustrated in figure 7. These intra-adiabat variations fall within the MCMC uncertainty range already indicated for each adiabat (represented by the box ranges in figure 7). Within this narrower parameter range for each adiabat, the simulated XRTS spectra exhibit minimal variation, resulting in parameter convergences consistent with those shown in figure 7. This is because the MCMC analysis on the simulated XRTS spectra is deterministic, meaning analysis on identical XRTS spectra will produce the same results.

For the higher adiabat targets, the forward detector converges around lower densities and higher temperatures than expected. This discrepancy can be understood by evaluating the expected energy shift of the electron plasma wave resonance using equation (9). As illustrated in figure 8, the lowest adiabat target exhibits a sharp distribution with a plasmon shift around ≈37 eV. In contrast, the higher adiabat targets display much broader plasmon shift distributions. Consequently, as observed in the x-ray scattering signals in figures 6(e) and (f), the plasmon peaks in the higher adiabats are very broad and closer to the elastic scattering signal. Part of this breadth is a result of the additional broadening due to the bandwidth of the incident x-ray probe. As the position of the plasmon peak constrains the electron density in the collective scattering regime, the analysis of these forward scattering spectra struggles to converge around the expected electron density and instead compensates by finding higher electron temperatures.

In comparison, the forward scattering analysis for the lowest adiabat target converges around an electron density of $(6-8) \times 10^{23}\,cm^{-3}$. While this is higher than the mass-averaged simulation value of 5.9×10^{23} cm^{-3}, it aligns with the most probable compressed shell density conditions as observed in the simulation probability distribution functions. This discrepancy raises the question of whether, in

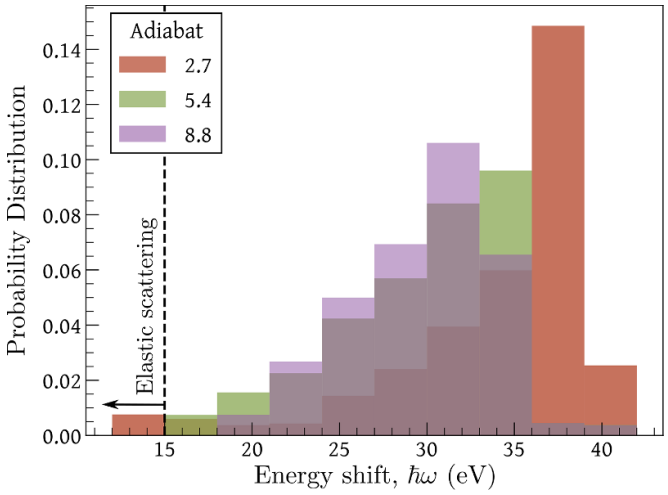

Figure 8. Probability distribution functions of the energy shift determined by the plasmon dispersion relation (equation (9)) for each target. As in figure 3(b), the energy shift is weighted by the electron density in each region and is determined for a 2 keV incident x-ray energy with a scattering angle of 40°. A bin size of 3 eV bin^{-1} is utilised based on the assumed spectral resolution of the detector. The black dashed vertical line indicates the highest observed energy of the elastic scattering peak.

more realistic simulations that factor in intermediate-mode perturbations, it is more appropriate to compare the MCMC averages to the most probable conditions rather than the mass-averaged values. This trend is also observed in the backward detector analysis across all targets. The non-collective scattering converges around lower temperatures than the mass-averaged values, but in closer alignment with the most probable temperature conditions. For the lowest target adiabat, the closest agreement with the most probable conditions is achieved by using the temperature information from the backward detector and the density information from the forward detector. This was the intention of the proposed dual-detector approach, where one detector is sensitive to temperature while the other is sensitive to electron density.

This investigation into the x-ray scattering produced by three different target adiabat conditions has highlighted the impact intermediate-mode perturbations have on the inferred conditions. Primarily, the effect these perturbations have on the electron density distribution presents a challenge in resolving collective scattering features. Initial investigations into fielding such a diagnostic platform may, therefore, focus on lower adiabat target designs or those with expected narrower electron density distributions. Additionally, better agreement between the forward detector analysis and simulations may be achieved if a narrower bandwidth x-ray probe can be assumed, which would reduce the inherent broadening on the plasmon peaks.

Future work will investigate the effect of higher-mode perturbations ($\ell > 50$) on the x-ray scattering spectrum and subsequent analysis. These perturbations may introduce interfacial mixing between different material layers in the ICF target, complicating the scattering analysis by making it inappropriate to assume a single DT region in the fitting process. However, due to the reduction of the SSD bandwidth in the currently investigated simulations, resulting in more perturbed implosions than nominally expected, higher-mode perturbations are not anticipated to significantly affect the in-flight DT density distribution. Therefore, apart from the potential material mixing, these perturbations are unlikely to substantially impact the overall analysis presented in this work.

6. Conclusions

This work has demonstrated the potential offered by the development of an XRTS diagnostic platform for direct-drive cryogenic inertial confinement fusion implosions in resolving the in-flight compressed shell conditions. Spatially-integrated XRTS spectra were calculated for 2D simulated conditions with varying target adiabats at two-thirds convergence. This methodology successfully distinguished between high and low adiabat implosion conditions using both 1-D and 2D simulations. The capability to discern the compressed shell conditions despite the introduction of intermediate-mode perturbations provides confidence in the feasibility of fielding this diagnostic platform on realistic capsule implosions.

Data availability statement

The data cannot be made publicly available upon publication because the cost of preparing, depositing and hosting the data would be prohibitive within the terms of this research project. The data that support the findings of this study are available upon reasonable request from the authors.

Acknowledgments

This material is based upon work supported by the Department of Energy [National Nuclear Security Administration] University of Rochester 'National Inertial Confinement Fusion Program' under Award Number DE-NA0004144. We also acknowledge support from the National Science Foundation under Award PHY-2308844.

This report was prepared as an account of work sponsored by an agency of the U.S. Government. Neither the U.S. Government nor any agency thereof, nor any of their employees, makes any warranty, express or implied, or assumes any legal liability or responsibility for the accuracy, completeness, or usefulness of any information, apparatus, product, or process disclosed, or represents that its use would not infringe privately owned rights. Reference herein to any specific commercial product, process, or service by trade name, trademark, manufacturer, or otherwise does not necessarily constitute or imply its endorsement, recommendation, or favoring by the U.S. Government or any agency thereof. The views and opinions of authors expressed herein do not necessarily state or reflect those of the U.S. Government or any agency thereof.

ORCID iDs

H Poole https://orcid.org/0000-0002-2206-5927
I Golovkin https://orcid.org/0000-0002-4985-0386
S X Hu https://orcid.org/0000-0003-2465-3818
T Walton https://orcid.org/0000-0002-2486-8328

References

[1] Abu-Shawareb H *et al* 2024 *Phys. Rev. Lett.* **132** 065102
[2] Abu-Shawareb H *et al* 2022 *Phys. Rev. Lett.* **129** 075001
[3] Gopalaswamy V *et al* 2024 *Nat. Phys.* **20** 1217
[4] Grim G *et al* 2013 *Phys. Plasmas* **20** 056320
[5] Frenje J 2020 *Plasma Phys. Control. Fusion* **62** 023001
[6] Mannion O M *et al* 2022 *Phys. Rev.* E **105** 055205
[7] Kilkenny J *et al* 2016 *Fusion Sci. Technol.* **69** 420
[8] Rygg J *et al* 2014 *Phys. Rev. Lett.* **112** 195001
[9] Hamza A *et al* 2016 *Fusion Sci. Technol.* **69** 395
[10] Lindl J 1995 *Phys. Plasmas* **2** 3933
[11] Kritcher A *et al* 2024 *Phys. Rev.* E **109** 025204
[12] Marinak M M, Kerbel G, Gentile N, Jones O, Munro D, Pollaine S, Dittrich T and Haan S 2001 *Phys. Plasmas* **8** 2275
[13] Radha P B *et al* 2005 *Phys. Plasmas* **12** 056307
[14] Gopalaswamy V *et al* 2019 *Nature* **565** 581
[15] Lees A *et al* 2023 *Phys. Plasmas* **30** 012709
[16] Lindl J D 1998 Inertial confinement fusion: the quest for ignition and energy gain using indirect drive (Springer)
[17] Betti R and Hurricane O A 2016 *Nat. Phys.* **12** 435
[18] Goncharov V N *et al* 2014 *Phys. Plasmas* **21** 056315
[19] Craxton R S *et al* 2015 *Phys. Plasmas* **22** 110501
[20] Landen O L *et al* 2020 *High Energy Density Phys.* **36** 100755
[21] Melvin J, Lim H, Rana V, Cheng B, Glimm J, Sharp D H and Wilson D C 2015 *Phys. Plasmas* **22** 022708
[22] Dittrich T R *et al* 2014 *Phys. Rev. Lett.* **112** 055002
[23] Radha P B *et al* 2016 *J. Phys.: Conf. Ser.* **688** 012006
[24] Rinderknecht H G, Casey D T, Hatarik R, Bionta R M, MacGowan B J, Patel P, Landen O L, Hartouni E P and Hurricane O A 2020 *Phys. Rev. Lett.* **124** 145002
[25] Mannion O M *et al* 2021 *Phys. Plasmas* **28** 042701
[26] Smalyuk V A *et al* 2019 *Plasma Phys. Control. Fusion* **62** 014007
[27] Landen O 2024 *High Energy Density Phys.* **51** 101102
[28] Glenzer S H and Redmer R 2009 *Rev. Mod. Phys.* **81** 1625
[29] Kraus D *et al* 2016 *Phys. Rev.* E **94** 011202(R)
[30] Kritcher A L, Döppner T, Fortmann C, Ma T, Landen O L, Wallace R and Glenzer S H 2011 *Phys. Rev. Lett.* **107** 015002
[31] Regan S P *et al* 2012 *Phys. Rev. Lett.* **109** 265003
[32] Falk K *et al* 2013 *Phys. Rev.* E **87** 043112
[33] MacFarlane J J, Golovkin I, Wang P, Woodruff P R and Pereyra N A 2007 *High Energy Density Phys.* **3** 181
[34] Salpeter E E 1960 *Phys. Rev.* **120** 1528
[35] Poole H *et al* 2022 *Phys. Plasmas* **29** 072703
[36] Olver F W J (eds) NIST Digital Library of Mathematical Functions Release 1.2.3 of 2024-12-15 (available at: https://dlmf.nist.gov/)
[37] Gregori G, Glenzer S H, Rogers F J, Pollaine S M, Landen O L, Blancard C, Faussurier G, Renaudin P, Kuhlbrodt S and Redmer R 2004 *Phys. Plasmas* **11** 2754
[38] Thiele R, Bornath T, Fortmann C, Höll A, Redmer R, Reinholz H, Röpke G, Wierling A, Glenzer S H and Gregori G 2008 *Phys. Rev.* E **78** 026411
[39] Collins T J B *et al* 2022 *Phys. Plasmas* **29** 012702
[40] Marozas J A *et al* 2018 *Phys. Plasmas* **25** 056314
[41] Delettrez J, Epstein R, Richardson M C, Jaanimagi P A and Henke B L 1987 *Phys. Rev.* A **36** 3926
[42] Hu S X, Collins L A, Goncharov V N, Kress J D, McCrory R L and Skupsky S 2015 *Phys. Rev.* E **92** 043104
[43] Hu S X, Collins L A, Goncharov V N, Boehly T R, Epstein R, McCrory R L and Skupsky S 2014 *Phys. Rev.* E **90** 033111
[44] Cao D, Moses G and Delettrez J 2015 *Phys. Plasmas* **22** 082308
[45] Laboratory for Laser Energetics 1999 *LLE Review Quarterly Report* (University of Rochester, Rochester, NY) vol 78 p 62
[46] Sawada H *et al* 2007 *Phys. Plasmas* **14** 122703
[47] Golovkin I, MacFarlane J J, Woodruff P, Hall I, Gregori G, Bailey J, Harding E, Ao T and Glenzer S H 2013 *High Energy Density Phys.* **9** 510
[48] Gregori G, Glenzer S H, Rozmus W, Lee R W and Landen O L 2003 *Phys. Rev.* E **67** 026412
[49] Kasim M, Galligan T P, Topp-Mugglestone J, Gregori G and Vinko S M 2019 *Phys. Plasmas* **26** 112706
[50] Poole H *et al* 2024 *Phys. Rev. Res.* **6** 023144